

# From superconducting fluctuations to the bosonic limit in the response functions above the critical temperature

G.C. Strinati, P. Pieri<sup>a</sup>, and C. Lucheroni

Dipartimento di Fisica, Sezione INFM Università di Camerino, 62032 Camerino, Italy

Received 8 October 2002

Published online 29 November 2002 – © EDP Sciences, Società Italiana di Fisica, Springer-Verlag 2002

**Abstract.** The density, current, and spin response functions are investigated *above* the critical temperature  $T_c$  for a system of three-dimensional fermions interacting *via* an attractive short-range potential, as the strength of this potential is varied from weak to strong coupling. In the strong-coupling (bosonic) limit, we identify the dominant diagrammatic contributions for a “dilute” system of composite bosons which form as bound-fermion pairs, by giving appropriate prescriptions for mapping bosonic onto fermionic diagrams. We then extrapolate these contributions to the weak-coupling limit and compare them with the ordinary (Aslamazov-Larkin, Maki-Thompson, and density of states) terms occurring in the theory of superconducting fluctuations for a clean system above the critical temperature. Specifically, we show that in the strong-coupling limit, at the zeroth order in the diluteness parameter for the composite bosons, the Aslamazov-Larkin term represents formally the dominant contribution to the density and current response functions, while the Maki-Thompson and density of states terms are strongly suppressed. Corrections to the Aslamazov-Larkin term are further identified *via* the above mapping prescriptions at the next order in the diluteness parameter for the composite bosons, where the residual mutual interaction appears explicitly. Numerical comparison of the Aslamazov-Larkin diagram and its leading corrections is presented for a range of temperature above  $T_c$  over the whole coupling region. The spin response function is also examined, and it is found to be correctly suppressed in the strong-coupling limit only when appropriate sets of diagrams are considered simultaneously, thus providing a criterion for grouping diagrammatic contributions to the response functions.

**PACS.** 74.40.+k Fluctuations (noise, chaos, nonequilibrium superconductivity, localization, etc.) – 74.20.-z Theories and models of superconducting state – 05.30.Jp Boson systems

## 1 Introduction

Response functions constitute an essential tool for connecting experimentally measurable quantities with the theoretical description of a condensed-matter system. Specifically, knowledge of density, current, spin, and heat response functions allows one to test the relevance of the degrees of freedom which are selected for an approximate description of a complex system. In particular, for superconductors the current response function plays a special role since the Meissner effect can be demonstrated by examining its behavior [1].

Within the standard BCS (weak-coupling) theory, the transverse current response function below the critical temperature is represented as a particle-hole bubble in terms of normal and anomalous single-particle propagators [1,2]. Above the critical temperature, the noninteracting Fermi gas expression is correspondingly obtained,

with no sign of superconductivity being evidenced when approaching the transition from above.

In the weak-coupling limit, precursor effects of superconductivity *above* the critical temperature have been considered, by introducing *pairing fluctuations* in the Fermi gas due to the same attractive interaction which is responsible for the formation of the superconducting state below the critical temperature. In this way, the so-called Aslamazov-Larkin (AL) [3], Maki-Thompson (MT) [4], as well as the density of states (DOS) contributions have been evaluated and tested against experimental data, for superconducting samples of reduced dimensionality [5] and for strongly anisotropic cuprate superconductors in the overdoped region [6].

No corresponding analysis has, however, been performed in the strong-coupling limit, where composite bosons form due to the strong fermionic attraction. Purpose of this paper is to provide this analysis, by setting up a formal classification of the diagrammatic structure for the response functions that holds specifically in the

---

<sup>a</sup> e-mail: pierbiagio.pieri@unicam.it

strong-coupling limit. In this way, one is able to cover the whole interaction range from weak to strong coupling, by merging the two alternative approaches (holding separately in the weak- and strong-coupling regimes) through the intermediate-coupling region. This merging appears altogether nontrivial, in that two different small parameters (namely, the Ginzburg and gas diluteness parameters) control the theory in weak and strong coupling.

The intermediate-coupling region might be specifically relevant for cuprate superconductors, for which the pairing is likely to be in an *intermediate* regime between overlapping Cooper pairs and non-overlapping composite bosons. In fact, the small value of the (superconducting) coherence length and the presence of a pseudogap above the critical temperature in the underdoped region [7, 8] have suggested a *crossover* scenario, from a weak-coupling regime with Cooper pairs forming and condensing at the critical temperature within a BCS description, toward a strong-coupling regime whereby preformed (composite) bosons exist above the superconducting critical temperature and Bose-Einstein condense below it [9–15].

In this context, it appears relevant to study how the response functions evolve toward the strong-coupling limit, by specifically examining how the response of the original Fermi system can be interpreted in terms of the response of an effective Bose system. This evolution of the response functions rests on the property that the fluctuation propagator, which constitutes the building block of fluctuation theory in the weak-coupling limit *above* the superconducting critical temperature, acquires the form of the propagator for composite bosons in the strong-coupling limit.

The dominant diagrammatic contributions to the response functions in the strong-coupling (bosonic) limit will be selected by relying on the diluteness condition of the system (which is automatically satisfied in the strong-coupling limit [12, 13]), in a similar fashion to what was done in reference [16] for the selection of the fermionic self-energy. In that reference, the diluteness condition was exploited to determine the bosonic propagator entering the fermionic self-energy, where the bosonic propagator couples with a fermionic propagator. In this paper, we apply the diluteness condition to the physical response functions, for which a description in terms of bosons will naturally emerge in the strong-coupling limit.

Although the above procedure is *a priori* complementary to the selection of fluctuation diagrams in the weak-coupling limit, it yet results into the *same* diagrams for the current (and density) response functions as far as the dominant contribution (over and above the free fermion contribution) is concerned. Specifically, the AL diagram turns out to yield the dominant contribution to the current (and density) response functions *both* in the weak-coupling limit (where it represents the main fluctuation effects close to the critical temperature) and in the strong-coupling limit (where it corresponds to a free-boson response). Corrections to the AL diagram will also be identified in the strong-coupling regime at the next-to-leading order in the diluteness parameter, thus including interaction effects between composite bosons. Calculation of these corrections

to the response functions will be further implemented numerically to show their relevance in a range of temperature above  $T_c$ .

Besides providing a detailed analysis of the current (and density) response functions, we will also examine the spin response function. We shall verify that the diagrams selected in the strong-coupling limit for the current (and density) response functions, give an identically vanishing contribution to the spin response function, since they correspond to spinless (composite) bosons. For obtaining a non vanishing contribution in the interesting intermediate-coupling region, therefore, the diagrams for the spin response function have to be selected in the weak-coupling region, paying, however, attention that their contribution has anyway to vanish in the strong-coupling limit. To this end, it will be shown how certain diagrammatic contributions have to be included simultaneously in an appropriate way.

We shall specifically consider a Fermi system with an attractive (point-contact) interaction in a three-dimensional continuum and *above* the superconducting critical temperature. No lattice or impurities effects will be taken into account. Consideration of the broken-symmetry case below the critical temperature is postponed to future work.

The plan of the paper is as follows. Section 2 discusses the current response function at the leading and next-to-leading order in the diluteness parameter for composite bosons. Section 3 considers the density and spin response functions. Section 4 presents the numerical results. Section 5 gives our conclusions.

## 2 Current response function

In this section, we identify the dominant diagrammatic contributions to the current response function for a system of fermions with an attractive interparticle interaction in the strong-coupling limit. The leading contribution turns out to coincide formally with the AL diagram, occurring in the standard theory of superconducting fluctuations above the critical temperature. Next-to-leading diagrams in the bosonic diluteness parameter are also considered, to include the effects of the residual interaction between the composite bosons in the strong-coupling limit. Additional diagrams (such as the MT and fermionic DOS contributions), which are usually considered in superconducting fluctuation theory, are further shown to be irrelevant in the strong-coupling limit.

The systematic procedure for selecting the contributions to the response functions which are dominant *in the strong-coupling limit* rests on certain integrals (that contain products of fermionic single-particle Green's functions) acquiring a particularly simple form in the strong-coupling limit, and on the standard classification of bosonic diagrams in the dilute limit [17]. In this way, the contributions to the response functions are organized in powers of the diluteness parameter as well as of the (inverse of the) fermionic chemical potential. The property of the fermionic chemical potential of being the largest

energy scale in the strong-coupling limit, in fact, considerably simplifies dealing with this limit.

The identification of the dominant diagrammatic contributions to the response functions for a system of fermions in the strong-coupling limit could proceed in two ways. Either, one may consider all possible *fermionic* diagrams and estimate their relative contributions by relying on the simplifying features mentioned above; or, one may start directly from the *bosonic* diagrams for a system of true bosons and construct the corresponding diagrams for composite bosons, where remnants of the underlying fermionic degrees of freedom explicitly appear. We shall develop below the latter approach, which has by construction the advantage of identifying the important contributions to the response functions in the strong-coupling limit.

Detailed knowledge of the fermionic attractive interaction is not required for studying the evolution from weak to strong coupling. One may accordingly consider a “contact” potential  $v_0 \delta(\mathbf{r})$ , where  $v_0$  is a negative constant. A suitable regularization is required in this case to remove divergences in the diagrammatic structure. In three dimensions, it is common practice to introduce the fermionic *scattering length*  $a_F$  defined *via* (we set  $\hbar$  and Boltzmann’s constant equal to unity throughout)

$$\frac{m}{4\pi a_F} = \frac{1}{v_0} + \int \frac{d\mathbf{k}}{(2\pi)^3} \frac{m}{k^2}, \quad (2.1)$$

where  $\mathbf{k}$  is a wave vector and  $m$  the fermionic mass. The ultraviolet divergence on the right-hand side of equation (2.1) is compensated by letting  $v_0 \rightarrow 0^-$  in a suitable way, while keeping  $a_F$  finite. This is achieved by introducing an ultraviolet cutoff  $k_0$  and choosing  $v_0$  such that [16]

$$v_0 = -\frac{2\pi^2}{mk_0} - \frac{\pi^3}{ma_F k_0^2}, \quad (2.2)$$

with  $k_0 \rightarrow \infty$  eventually. The evolution from weak to strong coupling can thus be tuned by varying the scattering length  $a_F$ , which is negative in the weak-coupling regime (where a bound-state has not yet appeared in the associated two-body problem) and positive in the strong-coupling (bosonic) regime (where  $a_F$  coincides with the bound-state radius).

It was discussed in reference [16] that the explicit form (2.2) for  $v_0$  considerably simplifies the structure of the associated many-body perturbation theory. It was shown there that the effects of the interaction survive *only* in the particle-particle ladder depicted in Figure 1a, while connections among different ladders (as well as other links required to form the fermionic self-energy) are provided by the fermionic bare single-particle Green’s functions. In the context of the response functions considered in the present paper, a current (or density or spin) vertex made by fermionic single-particle Green’s functions (*cf.* Fig. 1b) is further required to connect the external (electromagnetic) disturbance with the structure of the fermionic two-particle Green’s function.

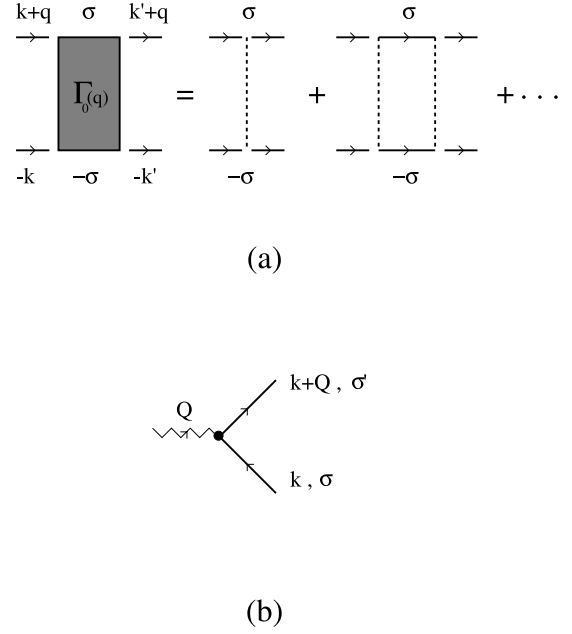


**Fig. 1.** (a) Particle-particle ladder, where full and broken lines represent fermionic bare single-particle Green’s functions and interactions, respectively (four-momenta and spin labels are indicated); (b) Current (or density or spin) vertex connecting the external (electromagnetic) disturbance to the fermionic two-particle Green’s function.

The general expression of the particle-particle ladder of Figure 1a for any temperature and value of  $a_F$  reads [16]:

$$\Gamma_0(q) = - \left\{ \frac{m}{4\pi a_F} + \int \frac{d\mathbf{k}}{(2\pi)^3} \right. \\ \left. \times \left[ \frac{1 \tanh(\beta\xi(\mathbf{k})/2) + \tanh(\beta\xi(\mathbf{k}-q)/2)}{2(\xi(\mathbf{k}) + \xi(\mathbf{k}-q) - i\omega_\nu)} - \frac{m}{k^2} \right] \right\}^{-1} \quad (2.3)$$

with the four-vector notation  $q \equiv (\mathbf{q}, \omega_\nu)$ , where  $\mathbf{q}$  is a wave vector,  $\omega_\nu = 2\nu\pi\beta^{-1}$  ( $\nu$  integer) a bosonic Matsubara frequency,  $\beta = 1/T$  the inverse temperature, and  $\xi(\mathbf{k}) = \mathbf{k}^2/(2m) - \mu$  ( $\mu$  being the fermionic chemical potential). This expression acquires a particularly simple form in the strong- and weak-coupling limits.

In the strong-coupling limit,  $\mu$  approaches the value  $-\epsilon_0/2$  where  $\epsilon_0 = (ma_F^2)^{-1}$  is the binding energy of the associated two-body problem. As  $\epsilon_0$  increases without bound in strong coupling, at any finite temperature we may consider the limit  $\beta\mu \rightarrow -\infty$  in equation (2.3), thus obtaining the *polar structure* [16]:

$$\Gamma_0(q) \cong -\frac{8\pi}{m^2 a_F} \frac{1}{i\omega_\nu - \frac{\mathbf{q}^2}{4m} + \mu_B} \quad (2.4)$$

where  $\mu_B = 2\mu + \epsilon_0$ . Apart from the residue being different from unity, this expression has the form of a free propagator for (composite) bosons with mass  $m_B = 2m$  and chemical potential  $\mu_B$ . Note that equation (2.4) holds provided  $|\omega_\nu| \ll \epsilon_0$  and  $\mathbf{q}^2/(4m) \ll \epsilon_0$ , which can be satisfied

for all relevant values of  $\omega_\nu$  and  $\mathbf{q}$  when  $\epsilon_0$  is sufficiently large.

In the weak-coupling limit, on the other hand, the chemical potential is (slightly) smaller than the Fermi energy  $\epsilon_F = k_F^2/(2m)$  ( $k_F$  being the Fermi wave vector) for temperatures much smaller than  $\epsilon_F$  itself. In this case, the particle-particle ladder (2.3) acquires the form characteristic of superconducting fluctuation theory [3]:

$$\Gamma_0(q) \cong \frac{1}{N_0} \frac{1}{\frac{T-T_c}{T_c} + \eta \mathbf{q}^2 + \gamma |\omega_\nu|} \quad (2.5)$$

where  $N_0$  is the free-fermion density of states at the Fermi level (per spin component),  $(T-T_c) \ll T_c$  where  $T_c$  is here the BCS critical temperature,  $\gamma = \pi/(8T_c)$ , and

$$\eta = \frac{7\zeta(3)}{48\pi^2} \left( \frac{k_F}{mT_c} \right)^2 \quad (2.6)$$

in three dimensions ( $\zeta(3) \approx 1.202$  being the Riemann zeta function of argument 3).

On physical grounds, one expects the response functions in the strong-coupling limit of the original Fermi system to be expressed *entirely* in terms of composite-boson structures, namely, bosonic propagators and vertices. As anticipated in the Introduction, the evolution of the response functions from strong to weak coupling discussed in the present paper rests on the fact that the particle-particle ladder (which in the strong-coupling limit has the form (2.4) of a composite-boson propagator) becomes itself the building block of fluctuation theory in the weak-coupling limit (*cf.* Eq. (2.5)).

Before identifying the relevant bosonic diagrams for the current response function, it is useful to establish a procedure to map a given bosonic diagram onto a corresponding set of fermionic diagrams. To this end, we proceed in a *heuristic* way and formulate the following *prescriptions*: (i) Remove from the given bosonic diagram the two outer vertices representing the bosonic coupling to the external field, thus obtaining a bosonic diagram “open” at its ends; (ii) Replace the bare bosonic propagators by the particle-particle ladders (2.3); (iii) Connect the ensuing (fermionic) diagram to the fermionic vertex of Figure 1b representing the fermionic coupling to the external field; (iv) Connect eventually the remaining dangling ends of the particle-particle ladders among themselves, in accordance with their spin structure.

In this way, besides the fermionic diagrams which correctly reproduce the value of the original bosonic diagram in the strong-coupling limit, additional fermionic diagrams may result which do not have a bosonic analogue in the strong-coupling limit and whose value is accordingly suppressed in this limit. These additional diagrams will consistently be dismissed when mapping the original bosonic diagrams onto the associated fermionic diagrams.

## 2.1 Leading diagrams

For a system of noninteracting bosons, the current response function is depicted diagrammatically in Figure 2a.

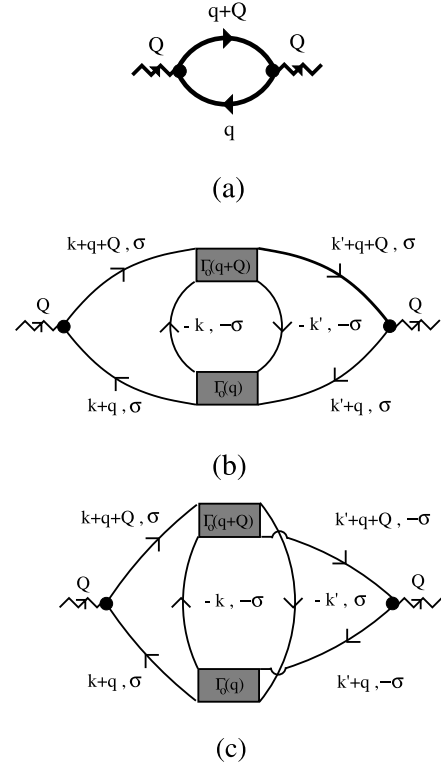


**Fig. 2.** (a) Current response function for an ideal Bose gas above the Bose-Einstein temperature, where thick lines represent bosonic bare single-particle Green's functions; (b)–(c) Corresponding current response function for a system of composite bosons.

This diagram represents the leading contribution to the current response function also for a system of bosons interacting *via* a (repulsive) finite-range potential at sufficiently *low density*.

With the prescriptions listed above, the fermionic diagrams of Figures 2b and c are generated from the bosonic diagram of Figure 2a, with a degeneracy factor of 2 each, due to the fermionic spin multiplicity. (An additional diagram, which corresponds to a self-energy decoration of both bare fermionic propagators in the fermionic particle-hole bubble, is also generated according to the above prescriptions. Since this diagram does not have a bosonic analogue in the strong-coupling limit, it will not be considered in the following according to the above discussion.) Although the two diagrams 2b and c are topologically not equivalent, their expressions coincide for particle-particle ladders corresponding to a point-contact potential. We thus consider only one of these diagrams (say, diagram 2b) with a multiplicity factor of 4.

This diagram contains two (vector) factors of the type:

$$\mathbf{J}(q, Q) = \frac{1}{\beta} \sum_{\omega_n} \int \frac{d\mathbf{k}}{(2\pi)^3} \frac{[2(\mathbf{k} + \mathbf{q}) + \mathbf{Q}]}{2m} \times \mathcal{G}^0(-k) \mathcal{G}^0(k+q) \mathcal{G}^0(k+q+Q) \quad (2.7)$$

where  $Q \equiv (\mathbf{Q}, \Omega_\nu)$  and  $k \equiv (\mathbf{k}, \omega_n)$  are bosonic and fermionic four-vectors, respectively, and  $\mathcal{G}^o(k) = (i\omega_n - \xi(\mathbf{k}))^{-1}$  is a fermionic *bare* propagator ( $\omega_n = (2n+1)\pi\beta^{-1}$  ( $n$  integer) being a fermionic Matsubara frequency). Symmetry arguments show that  $\mathbf{J}(q, Q)$  is directed along  $(2\mathbf{q} + \mathbf{Q})$ , allowing us to set

$$\mathbf{J}(q, Q) = \frac{(2\mathbf{q} + \mathbf{Q})}{2m} C(q, Q). \quad (2.8)$$

The (scalar) factor  $C(q, Q)$  can be readily evaluated in the strong-coupling limit for vanishing external four-vector ( $Q = 0$ ). In this limit, the Fermi functions originating from the sum over  $\omega_n$  in equation (2.7) vanish *exponentially* like  $\exp(-\beta|\mu|)$ , yielding

$$C(q, Q = 0) \approx -\frac{m^{3/2}}{16\pi} \frac{1}{\sqrt{2|\mu|}} \quad (2.9)$$

at the leading order in  $|\omega_\nu/\mu|$  and  $\mathbf{q}^2/(2m|\mu|)$ . With these approximations, and using the expression (2.4) for the particle-particle ladder in the strong-coupling limit, the value of the diagram of Figure 2b for  $Q = 0$  becomes (the “static” limit with  $\Omega_\nu = 0$  and  $\mathbf{Q} \rightarrow 0$  is implied):

$$\begin{aligned} \chi_j(Q = 0) &\cong -4 \frac{1}{m^2} \frac{m^3}{(16\pi)^2} \frac{1}{2|\mu|} \left( \frac{8\pi}{m^2 a_F} \right)^2 \\ &\times \frac{1}{\beta} \sum_{\omega_\nu} \int \frac{d\mathbf{q}}{(2\pi)^3} \frac{\mathbf{q}\mathbf{q}}{\left( i\omega_\nu - \frac{\mathbf{q}^2}{4m} + \mu_B \right)^2} \quad (2.10) \end{aligned}$$

where the overall minus sign complies with the definition of the current response function  $\chi_j$ , the factor of 4 represents the degeneracy of the diagram, and the remaining factors stem from equations (2.9) and (2.4), in the order. Apart from the degeneracy factor of 4, expression (2.10) coincides with the  $Q = 0$  limit of the current response function for a system of (composite) bosons with mass  $m_B = 2m$  and chemical potential  $\mu_B$ , when for  $|\mu|$  one uses the value  $(2ma_F^2)^{-1}$  which holds in the strong-coupling limit. This response function then equals  $-n_B/m_B$ , where the bosonic density  $n_B = n/2$  is half the original fermionic density  $n$ . The degeneracy factor of 4 in equation (2.10) restores eventually the correct value  $-n/m$  for the diagonal component of the fermionic current response function, in accordance with the f-sum rule [18]. This is an explicit check that the heuristic prescriptions formulated above lead indeed to a meaningful mapping between bosonic and fermionic diagrams.

It is also worth noting that, when the expression (2.5) for the particle-particle ladder (valid in the weak-coupling limit close to  $T_c$ ) is used in diagram 2b and the expression (2.8) is also retained, one recovers the standard Aslamazov-Larkin contribution to the current response function [3], which represents the leading fluctuation contribution in the weak-coupling limit. This is a nontrivial result because the weak- and strong-coupling regimes admit entirely different classifications schemes based, respectively, on the Ginzburg and diluteness (gas) parameters.

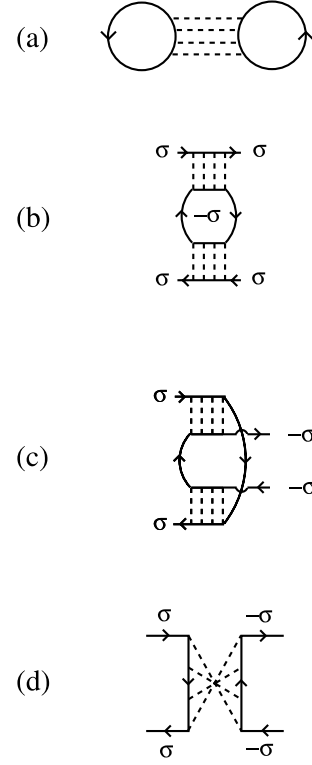


**Fig. 3.** (a) “Potential” from which the diagrams of Figures 2b and c are generated by the Baym’s prescriptions; (b)–(d) Fermionic effective two-particle interaction derived from the “potential” (a) (with spin labels corresponding to a contact interaction).

A lowest-order scheme to interpolate between weak and strong coupling for the current response function (and thus to address the interesting intermediate-coupling regime) can thus be set up by considering diagram 2b together with the fermionic bare particle-hole bubble. In this way, in the weak-coupling limit one retains the free-fermion result plus its AL fluctuation correction, while in the strong-coupling limit one recovers the free-boson result, which represent the dominant contributions in the respective limits.

It is worth mentioning that the AL diagrams 2b and 2c can be obtained also *via* the Baym’s prescriptions [19], also using the “potential” depicted in Figure 3a in fermionic language. Taking two successive functional derivatives with respect to the fermionic single-particle propagators (which, in this case, are meant to be self-consistent) yields, in fact, the fermionic effective two-particle interaction depicted in Figures 3b–d, which acts as the kernel of the Bethe-Salpeter equation for the two-particle Green’s function. Diagrams 2b and 2c then result by connecting, respectively, diagrams 3(b) and 3(c) with the fermionic vertex of Figure 1b, while connecting diagram 2d with the fermionic vertex of Figure 1b yields instead the Maki-Thompson diagram [4], to be considered in Section 2.3.

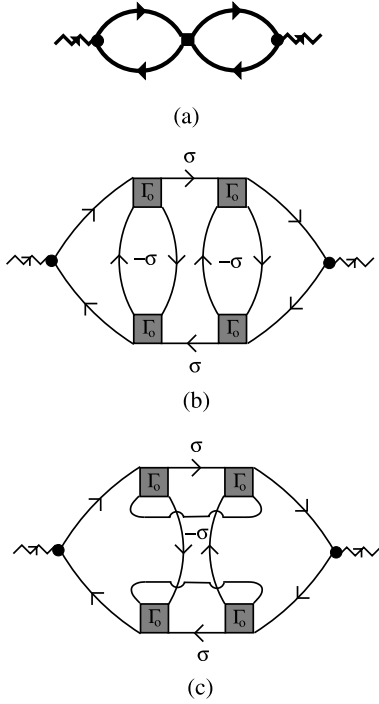


**Fig. 4.** (a) Next-to-leading bosonic diagram in the dilute limit; (b) Fermionic diagram corresponding to the bosonic diagram a; (c) Subleading diagram generated from diagram a.

## 2.2 Next-to-leading diagrams

The leading contribution to the current response function considered in Section 2.1 corresponds to non-interacting composite bosons. The residual interaction between composite bosons should, however, play an important role in the not-too-extreme strong-coupling regime [10,16]. For this reason, it is relevant to introduce the effects of the interaction between composite bosons in the physical response functions. This leads us to search for nontrivial corrections to the AL diagram, by examining diagrams of higher-order in the bosonic *diluteness parameter*  $n_B^{1/3} a_B$ , where  $a_B$  is the scattering length associated with the residual interaction between composite bosons [20].

A bosonic diagram, which is next-to-leading with respect to diagram 2a, is depicted in Figure 4a, where the dark square in the middle represents a (symmetrized) bosonic interaction [17]. The presence of an *additional bosonic cycle* in diagram 4a with respect to diagram 2(a) accounts, in fact, for an additional power in the diluteness parameter for high enough temperature [21]. A further bosonic diagram of the same order in the diluteness parameter can be obtained from diagram 2a, by dressing either one of the two bosonic propagators with a low-density self-energy (*cf.* Fig. 7 below), as in the theory of the interacting dilute Bose system [17]. The physical interplay of these two diagrams in the context of the density response function will be addressed in Section 4.

The bosonic diagram of Figure 4a can be mapped into a corresponding set of diagrams for the fermionic re-

sponse function(s), according to the rules developed in reference [16] for the interaction vertex and to the heuristic prescriptions stated above. In this way, one ends up with the two fermionic diagrams of Figs. 4b and c, with a degeneracy factor of 8 and 4, in the order, having also taken into account that expressions of topologically not equivalent diagrams may coincide for a fermionic point-contact potential. We will verify below that, while diagram 4b has a meaningful strong-coupling limit in terms of composite-boson propagators, diagram 4c lacks a bosonic representation and yields consistently a subleading contribution in this limit. For these reasons, one may retain diagram 4b and disregard diagram 4c to follow the evolution from strong to weak coupling.

To verify that to diagram 4b there corresponds a meaningful strong-coupling limit, we evaluate the central part of this diagram for  $Q = 0$  and obtain:

$$\frac{1}{\beta} \sum_{\omega_n''} \int \frac{dk''}{(2\pi)^3} \mathcal{G}^0(-k'') \mathcal{G}^0(k'' + q') \times \mathcal{G}^0(-k'' + q - q') \mathcal{G}^0(k'' + q') \approx \frac{(ma_F)^3}{16\pi} \quad (2.11)$$

where use has been made of the relation  $2|\mu| \approx \epsilon_0 = (ma_F^2)^{-1}$  that holds in this limit. The diagram 4b thus contains the factors

$$- \left( -\frac{m^2 a_F}{8\pi} \right)^2 \left( -\frac{8\pi}{m^2 a_F} \right)^4 \frac{(ma_F)^3}{16\pi} = -\frac{4\pi a_F}{m} \quad (2.12)$$

which arise, respectively, from the current vertex (*cf.* Eq. (2.9)), from the residue of the particle-particle ladder (*cf.* Eq. (2.4)), and from the expression (2.11), while the overall minus sign originates from the presence of three fermionic loops. In this way, the strength

$$v(0) = 4\pi a_F / m \quad (2.13)$$

of the residual interaction between composite bosons discussed in references [12,13] is correctly reconstructed, and diagram 4b is proved to give a faithful representation of the bosonic diagram of Figure 4a.

Further, the ratio of diagram 4c to diagram 4b can be estimated to be of the order

$$\frac{m}{a_F} \frac{(na_F^3)^2}{\frac{\partial n}{\partial \mu}}, \quad (2.14)$$

which is indeed much smaller than unity in the low-density limit ( $n_B^{1/3} a_B \ll 1$ ), provided the compressibility ( $\partial n / \partial \mu$ ) does not vanish [22].

It is again interesting to mention that diagram 4b (with a degeneracy factor of 8) can alternatively be obtained in fermionic language by: Considering the fermionic effective two-particle interaction depicted in Figures 3b and c to act *twice* in the two-fermion Green's function; Connecting the ensuing four diagrams with the fermionic vertex of Figure 1b; Recognizing the equivalence of these four diagrams; Summing eventually over the spin components. Diagram 4c, on the other hand is *not reducible* in

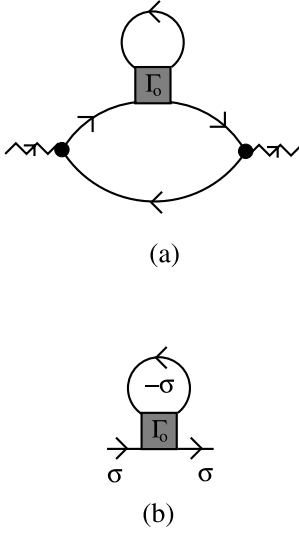


**Fig. 5.** (a) Fermionic DOS diagram for the response functions; (b) Self-energy diagram for a dilute Fermi gas.

the (fermionic) two-particle channel and corresponds to a choice of the fermionic effective two-particle interaction different from 3b and 3c.

In this way, we have identified the next-to-leading contributions to the dominant (AL) diagram, which take into account correlation effects among composite bosons in the strong-coupling limit.

### 2.3 Subleading diagrams

We finally consider additional diagrams (besides diagram 4(c) considered in Sect. 2.2) which are subleading in the strong-coupling limit. A noticeable example is the Maki-Thompson diagram, which is obtained by connecting the effective two-particle interaction of Figure 3d with the external coupling of Figure 1b. This diagram has been extensively studied in the weak-coupling limit in the context of the theory of superconducting fluctuations [4–6]. Since this diagram contains *only one* particle-particle ladder, it is expected to have no analogue in bosonic language (at least for the normal phase) and, consequently, not to contribute to the response functions in the strong-coupling limit. Upon evaluating the MT diagram for the current response function in the strong-coupling limit at  $Q = 0$ , however, one obtains the finite value  $n/m$  (including spin multiplicity).

This apparent contradiction can be overcome by considering also the fermionic density of states (DOS) diagram depicted in Figure 5a (with a multiplicity factor of 4), obtained by making the fermionic self-energy insertion of Figure 5b into the bare fermionic particle-hole bubble. In the strong-coupling limit, diagram 5(a) gives, in fact, the contribution  $-n/m$  to the  $Q = 0$  current response function, thus cancelling exactly the contribution of the MT diagram [23,24].

This example suggests that diagrams for the response functions may need to be *grouped into suitable sets*, in order to get a meaningful strong-coupling limit. The grouping procedure appears to be especially relevant for the spin response function, that ought to vanish in the strong-coupling limit for spinless composite bosons, as discussed in the next section.

## 3 Density and spin response functions

In this section, we complement the description of the strong-coupling limit by analyzing the density and spin response functions. We begin by considering the standard AL, MT, and fermionic DOS diagrams of the theory of superconducting fluctuations [5,6]. We next consider a specific example to show that a whole set of diagrams needs to be associated with a given subleading diagram, for the spin response function to be *exponentially suppressed* in the strong-coupling limit, as required on physical grounds for spinless composite bosons.

The contribution to the density response function from the AL diagram contains two (scalar) factors of the type

$$D(q, Q) = \frac{1}{\beta} \sum_{\omega_n} \int \frac{d\mathbf{k}}{(2\pi)^3} \mathcal{G}^0(-k) \mathcal{G}^0(k+q) \times \mathcal{G}^0(k+q+Q), \quad (3.1)$$

which can be readily evaluated in the strong-coupling limit for  $Q = 0$ , to give

$$D(q, Q = 0) \approx -\frac{m^2 a_F}{8\pi}. \quad (3.2)$$

This factor thus cancels the residue of the particle-particle ladder (2.4) in the strong-coupling limit, yielding for the density response function the following expression:

$$\chi_n(Q) \cong -4 \frac{1}{\beta} \sum_{\omega_\nu} \int \frac{d\mathbf{q}}{(2\pi)^3} \frac{1}{i\omega_\nu - \frac{\mathbf{q}^2}{4m} + \mu_B} \times \frac{1}{i\omega_\nu + i\Omega_\nu - \frac{(\mathbf{q}+Q)^2}{4m} + \mu_B}. \quad (3.3)$$

Here, the minus sign is due to the definition of the density response function and the factor of 4 accounts for the degeneracy of the diagram. In the “static” ( $\Omega_\nu = 0$  and  $\mathbf{Q} \rightarrow 0$ ) and “dynamic” ( $\mathbf{Q} = 0$  and  $\Omega_\nu \rightarrow 0$ ) limits this expression correctly produces the values  $-4\partial n_B/\partial\mu_B = -\partial n/\partial\mu$  and 0, in the order.

Concerning the spin response function, the contributions to  $\chi_{zz}$  from the AL diagrams 2b and 2c cancel each other *identically* for *all* coupling strengths (these diagrams, on the other hand, do not contribute to  $\chi_{xx}$  and  $\chi_{yy}$  owing to their spin structure). This is consistent with our previous result that, in the strong-coupling limit, the AL diagram gives an appropriate description of a system of composite bosons. One may further verify that the spin response function vanishes *identically* also for the corrections 4b to the AL diagram, a result which

is also expected since this diagram was selected in the strong-coupling limit.

The contributions to the ( $Q = 0$ ) density response function from the MT diagram 3(d) and the fermionic DOS diagram 5a do not cancel each other in the strong-coupling limit, contrary to the case of the current response function treated in Section 2.3. Rather, each of these diagrams gives the same finite contribution  $-ma_F^2 n_B = -n/(4|\mu|)$ , which however vanishes as  $|\mu|$  increases in the strong-coupling limit. In the strong-coupling limit, both MT and fermionic DOS diagrams are thus irrelevant also for the density response function.

The contributions to the spin response function  $\chi_{zz}$  from the MT and fermionic DOS diagrams cancel instead each other for  $Q = 0$  in the strong-coupling limit, since the MT contribution acquires an extra minus sign with respect to the DOS contribution. In particular, the spin response function, obtained by considering these two diagrams simultaneously, vanishes *exponentially* like  $\exp(-\beta|\mu|)$  when approaching the strong-coupling limit, due to the behavior of the Fermi functions in this limit. This is precisely what is expected on physical grounds, since a non-vanishing contribution to the spin response for spinless composite bosons should result only when the temperature is comparable with their binding energy and the composite bosons break apart. In this context, it is interesting to mention that the progressive vanishing of the spin susceptibility upon approaching the strong-coupling limit has been confirmed by Monte Carlo data for the negative-U Hubbard model [25], even though the predicted exponential behavior cannot be fully confirmed from the limited set of Monte Carlo data.

The above examples concerning the spin response for the AL, MT, and fermionic DOS diagrams (plus the correction 4(b) to the AL diagram) suggest that: (i) Diagrams selected in the strong-coupling regime according to the diluteness condition by considering the current response function, cannot be used to describe the spin response function, since they would yield a vanishing spin response function for all couplings. This implies that *additional* diagrams have unavoidably to be considered for a full description of the weak-coupling regime; (ii) These additional diagrams introduced in the weak-coupling regime (for instance, by counting powers of the Ginzburg parameter as in the theory of superconducting fluctuations) are necessarily subleading in the strong-coupling limit, as far as the current and density response functions are concerned. However, there is *a priori* no guarantee that they also result in an *exponentially* vanishing spin response function in the strong-coupling limit, as required on physical grounds. To make sure that this happens, suitable sets of diagrams need to be grouped in an appropriate way [24].

As a specific example, let us consider diagram 4c, which we concluded in Section 2.2 to be subleading as far as the current response is concerned. This diagram alone yields a contribution to the spin response function which is *not* exponentially vanishing in the strong-coupling limit. Additional diagrams have thus to be associated with diagram 4c, to obtain the correct exponential behavior of

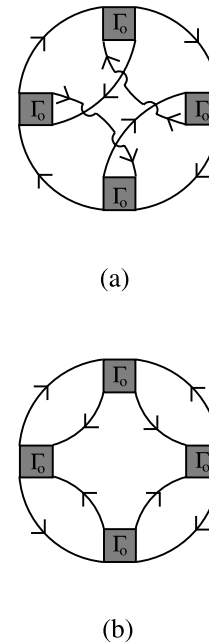


**Fig. 6.** (a)–(b) Diagrams for the thermodynamic potential, from which the contribution of Figure 4c to the static spin susceptibility can be derived.

the spin response function in the strong-coupling limit. To this end, we consider the two contributions to the thermodynamic potential depicted schematically in Figures 6a and b and perform all possible ( $Q = 0$ ) magnetic-field insertions in the fermionic single-particle propagators, as to get the “static” spin susceptibility (no additional contributions are obtained by making magnetic-field insertions inside the particle-particle ladder in the strong-coupling limit). In this way, two sets of six diagrams each result, which include, by construction, diagram 4c (counted twice, due to the equivalence of two diagrams for the case of a point-contact potential) plus decorations of the AL, MT, and fermionic DOS diagrams. In the strong-coupling limit (when all terms proportional to the Fermi functions are exponentially suppressed), it can indeed be shown that the contributions to the spin response function  $\chi_{zz}$  from the six diagrams obtained from Figure 6a (as well from the six diagrams obtained from Fig. 6b) add up to zero.

To summarize, we have argued that diagrams which have a meaningful strong-coupling limit as far as the current and density response are concerned, yield an *identically vanishing* contribution to the spin response function. Other diagrams that do not have a meaningful strong-coupling limit, on the other hand, give contributions to the spin response function in the strong-coupling limit which instead vanish *exponentially* like  $\exp(-\beta|\mu|)$  in the correct way, provided these diagrams are grouped into suitable sets, as shown explicitly by the examples considered above.

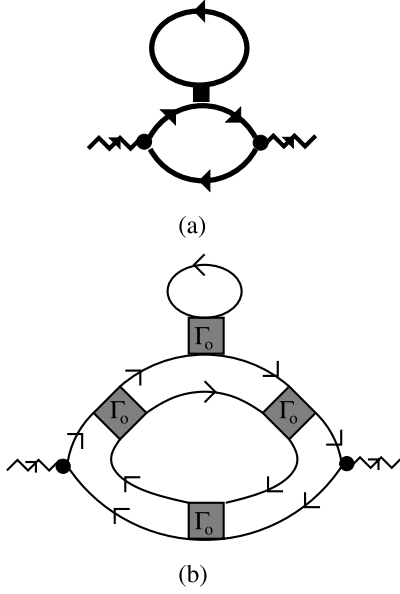


**Fig. 7.** (a) Density response function for an ideal Bose gas corrected by a self-energy insertion; (b) Corresponding density response function for a system of composite bosons made up of fermion pairs.

## 4 Numerical results

Having discussed on general grounds the diagrams that are relevant when addressing density, spin, and current response functions, in this section we investigate numerically the temperature dependence of the leading and sub-leading contributions to the density response function  $\chi_n$  in the “static” limit. This calculation is meant to provide us with a typical example for the relative contributions of higher-order diagrams with respect to the leading one.

Specifically, we shall consider three contributions to the density response function  $\chi_n$ , namely: (i) The density analogue of the AL diagram of Figure 2b, that we shall call AL1 for convenience; (ii) The density analogue of its leading correction of Figure 4b, that we shall call AL2 accordingly; (iii) The diagram of Figure 7b, which is derived [16] from the bosonic diagram of Figure 7a (with a degeneracy factor of 8), and which we shall call DOS2 as it represents the bosonic analogue of the fermionic DOS diagram of Figure 5a. As anticipated in Section 2.2, the two contributions AL2 and DOS2 are expected to be of the same order beyond AL1, for sufficiently large temperature above  $T_c$ .

These three contributions will be evaluated as a function of temperature above  $T_c$  for three representative values of the coupling strength  $(k_F a_F)^{-1}$  (namely, 1.33, 0.35,  $-0.40$ ), which are in the strong-, intermediate-, and weak-coupling regions, respectively. As the calculation proves to be altogether nontrivial, it will be schematically described in the following.

For given value of the coupling strength  $(k_F a_F)^{-1}$ , the input parameters  $T_c$  and  $\mu(T)$  to be used in the calculation are obtained according to the procedure described in refer-

ence [26]. Thus, the Thouless criterion  $\Gamma_0(q=0)^{-1} = 0$  in terms of the particle-particle ladder (2.3) is supplemented by the density equation relating the chemical potential  $\mu(T)$  to the density. In this way,  $T_c$  evolves from the BCS value in weak coupling to the Bose-Einstein temperature in strong coupling.

The contributions AL1, AL2, and DOS2 can be expressed in terms of three basic ingredients, namely, the particle-particle ladder  $\Gamma_0$  of equation (2.3), the three-fermion vertex

$$v(q) = \frac{1}{\beta} \sum_{\omega_n} \int \frac{d\mathbf{k}}{(2\pi)^3} \mathcal{G}^0(k+q)^2 \mathcal{G}^0(-k), \quad (4.1)$$

and the four-fermion vertex

$$u(q_1, q_2) = \frac{1}{\beta} \sum_{\omega_n} \int \frac{d\mathbf{k}}{(2\pi)^3} \mathcal{G}^0(-k)^2 \mathcal{G}^0(k+q_1) \mathcal{G}^0(k+q_2). \quad (4.2)$$

For instance, the contribution DOS2 to  $\chi_n$  is obtained as follows:

$$\begin{aligned} \chi(\text{DOS2}) = & \frac{1}{\beta^2} \sum_{\omega_{\nu_1} \omega_{\nu_2}} \int \frac{d\mathbf{q}_1}{(2\pi)^3} \int \frac{d\mathbf{q}_2}{(2\pi)^3} \\ & \times \Gamma_0(q_1)^3 v(q_1)^2 u(q_1, q_2) \Gamma_0(q_2). \end{aligned} \quad (4.3)$$

Here, the Matsubara sums contained in the terms  $v$  (Eq. (4.1)) and  $u$  (Eq. (4.2)) can be performed analytically. The remaining two Matsubara sums of equation (4.3) and the wave-vector integrals have instead to be performed numerically. The nested structure of the wave-vector integrals poses considerable numerical problems, since the integrals extending formally over an infinite range must in practice be truncated at some cutoff, so that the convergence of each individual integral depends on the convergence of others. In addition, there occurs a number of singularities (hidden mostly in the vertex  $u$  of equation (4.2)), which (albeit formally integrable) might in practice invalidate the whole numerical calculation. This divergence problem becomes apparent when the integrand of  $u$  is written in the following form (after the analytic sum over  $\omega_n$  has been performed):

$$\begin{aligned} & \frac{f'(-\xi(\mathbf{k}))}{A(k, q_1)B(k, q_2)} + \frac{1}{A^2(k, q_1)} \left[ \frac{f(-\xi(\mathbf{k}))}{B(k, q_2)} + \frac{f(\xi(\mathbf{k} + \mathbf{q}_1))}{C(k, q_1, q_2)} \right] \\ & + \frac{1}{B^2(k, q_1)} \left[ \frac{f(-\xi(\mathbf{k}))}{A(k, q_2)} - \frac{f(\xi(\mathbf{k} + \mathbf{q}_2))}{C(k, q_1, q_2)} \right]. \end{aligned} \quad (4.4)$$

Here,  $A(k, q_1) = \xi(\mathbf{k} + \mathbf{q}_1) + \xi(\mathbf{k}) - i\Omega_1$ ,  $B(k, q_2) = \xi(\mathbf{k} + \mathbf{q}_2) + \xi(\mathbf{k}) - i\Omega_2$ ,  $C(k, q_1, q_2) = \xi(\mathbf{k} + \mathbf{q}_1) - \xi(\mathbf{k} + \mathbf{q}_2) - i(\Omega_1 - \Omega_2)$ , and  $f$  is the Fermi distribution. A divergence clearly appears in the third and fifth terms of the expression (4.4) when  $q_1 = q_2$  and  $\Omega_1 = \Omega_2$ , since  $C = 0$  in this case irrespective of  $k$ . In addition, when  $q_1 = q_2$  and  $\Omega_1 = \Omega_2 = 0$ ,  $A$  and  $B$  could also vanish depending on the values of  $k$  and  $\mu$ . Other possibilities further occur, for a total of eight possible cases for which

terms of the expression (4.4) can individually diverge. Although these singularities eventually cancel each other, yielding a finite result, the numerical problem when approaching these singular values is evident.

An additional numerical problem concerns the intrinsic time scale of the calculation, that can be considerably large (of the order of one day for each data point reported in the following Figures 8–10 when a PC equipped with a single 1-GHz Pentium III processor is used). To reduce this time scale considerably, besides making use of symmetry properties such as

$$u(q_1, q_2) = u(q_2, q_1) \quad (4.5)$$

and

$$u(-q_1, -q_2) = u(q_1, q_2)^* , \quad (4.6)$$

we have resorted to parallel computation on a Beowulf cluster with 8 1-GHz Pentium III processors. In this way, the typical values to obtain each data point in Figures 8–10 has been approximately reduced to three to four hours.

The slow convergence of frequency sums and wave-vector integrals, related to the introduction of cutoffs as discussed above, has been dealt with as follows. Consider, for instance, a frequency sum which is conveniently cut at an upper frequency  $\bar{\omega}$ . The remaining contribution for  $\omega > \bar{\omega}$  can be calculated by transforming it into an integral:

$$\frac{1}{\beta} \sum_{\omega_\nu > \bar{\omega}} F(q, \omega_\nu) \rightarrow \int_{\bar{\omega}}^{\infty} \frac{d\omega}{2\pi} F(q, \omega) . \quad (4.7)$$

The ensuing improper integral can then be evaluated numerically using the mapping  $\omega \rightarrow 1/\omega$ , that transforms the improper integral into a proper one extending from  $\omega = 0$  to  $\omega = 1/\bar{\omega}$ . The same procedure can be applied to the wave-vector integrals as well. With this procedure, the dependence of the frequency sums and wave-vector integrals on the cutoff turns out to be much less critical than before.

Facing the divergence problem as in the expression (4.4), on the other hand, requires us to trade accuracy with velocity. Whenever possible, the divergences are located analytically and in the evaluation of the integral a small portion of the integration domain is excluded.

Finally, we mention that the DOS2 diagram suffers from an additional slow convergence when the factors  $\Gamma_0$  are summed over  $\omega_{\nu_1}$  and  $\omega_{\nu_2}$  (*cf.* Eq. (4.3)). This problem has been suitably alleviated by computing the frequency tail via the transformation  $\omega \rightarrow 1/\omega^2$ .

During code development, steps of the calculation were confronted (whenever possible) with analytic results that can be obtained in the strong-coupling limit, where the limiting forms of  $\Gamma_0$ ,  $v$ , and  $u$  hold (*cf.*, *e.g.*, Eqs. (2.4) and (2.11)). For example, in the strong-coupling the DOS2

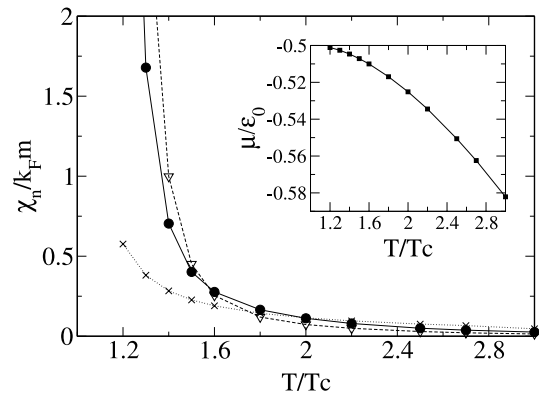


**Fig. 8.** Static limit of the density response function (in units of  $k_{FM}$ ) vs.  $T/T_c$  for  $(k_F a_F)^{-1} = 1.33$  (strong-coupling regime) corresponding to diagrams AL1 ( $\times$ ), AL2 ( $\bullet$ ), and DOS2 ( $\nabla$ ). In this case,  $T_c/\epsilon_0 = 0.065$ . The lines are guides to the eye and connect also points not shown in the graph. The inset shows the corresponding chemical potential (in units of  $\epsilon_0$ ) vs.  $T/T_c$ .

diagram has the factorized quadrature form

$$\frac{a_F \beta^2}{2m\pi^3} \int \frac{q^2 dq}{e^{\beta \xi_b(\mathbf{q})} - 1} \times \int \frac{q^2 dq}{\tanh\left(\frac{\beta \xi_b(\mathbf{q})}{2}\right) \sinh^2\left(\frac{\beta \xi_b(\mathbf{q})}{2}\right)} , \quad (4.8)$$

that has been explicitly used for checks, where  $\xi_b(\mathbf{q}) = \mathbf{q}^2/(4m_B) - \mu_B$  is the bosonic dispersion. In addition, external wave-vector integrations have been cutoff at large enough values such that the tails of the integrand proved irrelevant. The integrations were eventually performed over a mesh containing a number of points providing balance between numerical stabilization of the double integral and an affordable computation time scale.

The results of the numerical calculations are reported in Figures 8–10. Here, the static value  $\chi_n$  of the density response function corresponding to the three contributions AL1 (crosses), AL2 (full dots), and DOS2 (triangles) is plotted as a function of temperature above  $T_c$  for the three chosen values of the coupling strength  $(k_F a_F)^{-1}$ , each one representative of the coupling regimes of interest.

Note that all three plots of  $\chi_n$  vs.  $T/T_c$  show essentially the same pattern. Above a characteristic temperature that depends on  $(k_F a_F)^{-1}$ , AL1 becomes dominant over AL2 and DOS2, which in turn are comparable to each other, as anticipated when selecting the corresponding diagrams. One could identify this characteristic temperature as a kind of Ginzburg temperature  $T_G$ , since below  $T_G$  critical fluctuations become important and the perturbative (low-density) analysis presented in this paper breaks down. Below  $T_G$ , in fact, the contributions AL2 and DOS2 dominate over AL1, as Figures 8–10 show.

Note further that all three contributions diverge upon approaching  $T_c$  for any coupling. This divergence originates from the zero-frequency and low wave-vector structure of  $\Gamma_0(q) \sim (\mathbf{q}^2 + r)^{-1}$ , where  $r$  is a function of  $T$  that vanishes at  $T = T_c$ . The degree of divergence of each

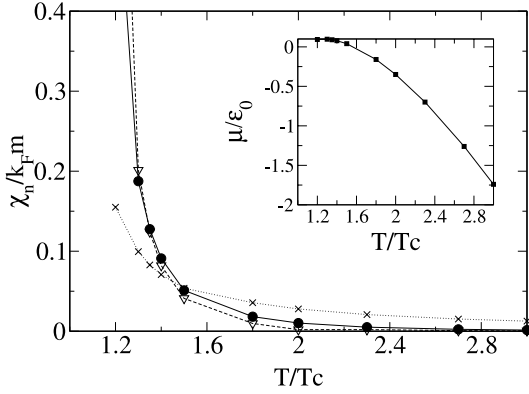


**Fig. 9.** Same as Figure 8 for  $(k_F a_F)^{-1} = 0.35$  (intermediate-coupling regime). In this case,  $T_c/\epsilon_0 = 1.07$ .

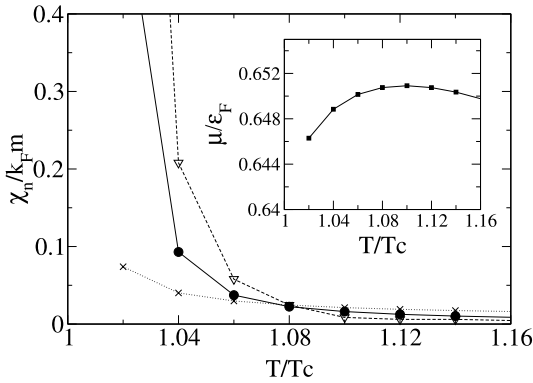


**Fig. 10.** Same as Figure 8 for  $(k_F a_F)^{-1} = -0.40$  (weak-coupling regime). In this case,  $T_c/\epsilon_F = 0.19$ . The inset shows the corresponding chemical potential (now in units of  $\epsilon_F$ ) vs.  $T/T_c$ .

diagram can be thus estimated by singling out the zero-frequency term from the frequency sum, whenever this term yields an infrared-divergent wave-vector integration. In this way, one obtains AL1  $\sim r^{-1/2}$ , AL2  $\sim r^{-1}$ , and DOS2  $\sim r^{-3/2}$ . These degrees of divergence, which are valid for any coupling, are indeed confirmed by the numerical results reported in Figures 8–10.

On similar grounds, an analytic estimate of  $T_G$  can be obtained in the strong-coupling regime, with the same approximation for  $\partial n/\partial \mu$  used for equation (2.14) [22]. In this regime, when  $T \gtrsim T_c$ , estimates of AL1, AL2, and DOS2 give, respectively,

$$\left(\frac{n_B}{1.63}\right) \frac{1}{(T - T_c)}, \quad (4.9)$$

$$v(0) \left(\frac{n_B}{1.63}\right)^2 \frac{1}{(T - T_c)^2}, \quad (4.10)$$

and

$$v(0) \frac{T_c}{3} \left(\frac{n_B}{1.63}\right)^2 \frac{1}{(T - T_c)^3}, \quad (4.11)$$

where  $v(0)$  is defined by equation (2.13). Note that the degrees of divergence upon approaching  $T_c$  are in agreement with the previous discussion. Defining  $T_1^a$  as the

temperature where AL1 equals AL2, from equations (4.9) and (4.10) it follows that

$$\frac{T_1^a - T_c}{T_c} = 2.33 n_B^{1/3} a_B, \quad (4.12)$$

in accordance with the estimate of the Ginzburg temperature  $T_G$  for a “dilute” Bose gas obtained in reference [21]. For  $(k_F a_F)^{-1} = 1.33$ ,  $n_B^{1/3} a_B = 0.39$  and  $T_1^a/T_c = 1.91$ , in good agreement with the numerical estimate  $T_1^n/T_c \simeq 2.00$  extracted from the data of Figure 8. In a similar way, defining  $T_2^a$  as the temperature where AL1 equals DOS2, from equations (4.9) and (4.11) it follows that

$$\left(\frac{T_2^a - T_c}{T_c}\right)^2 = 0.78 n_B^{1/3} a_B. \quad (4.13)$$

For  $(k_F a_F)^{-1} = 1.33$ , one finds  $T_2^a/T_c = 1.55$ , again in agreement with the numerical estimate  $T_2^n/T_c \simeq 1.80$  extracted from the data of Figure 8.

Equations (4.9–4.11) can also be used to estimate the ratios of DOS2 to AL2 and of AL2 to AL1 at a given temperature  $T \gtrsim T_c$ . For example, when  $T \simeq 2T_c$  the ratio of DOS2 to AL2 is estimated to be about 0.33, a value not too far from the numerical value 0.65 obtained from the data of Figure 8. In the same way, the ratio of AL2 to AL1 is estimated to be  $2.33 n_B^{1/3} a_B$ , that gives the value 0.9 when  $(k_F a_F)^{-1} = 1.33$ , in agreement with the numerical result 0.97 obtained from the data of Figure 8.

Finally, it is interesting to compare  $T_G$  thus obtained with the pseudogap crossover temperature  $T_0^*$  calculated in reference [26] (*cf.* Fig. 10 therein). While  $T_G$  and  $T_0^*$  essentially coincide in weak coupling, for larger coupling the two temperatures become well separated. For instance, already at the intermediate-coupling value  $(k_F a_F)^{-1} = 0.35$  our plots show  $T_G \simeq 1.5T_c$  while from reference [26]  $T_0^* \simeq 4T_c$ , with the ratio  $T_0^*/T_G$  becoming even larger at stronger coupling. We thus conclude that, in the intermediate-to-strong-coupling regime, our low-density analysis is applicable in a physically interesting temperature range where pseudogap effects are important and yet critical fluctuations are negligible. On the other hand, in weak coupling the critical and pseudogap regions seem to coincide, thus invalidating in practice any diagrammatic approach in the temperature range of physical interest.

## 5 Discussion and concluding remarks

In this paper, we have examined the evolution from weak to strong coupling of the response functions for a three dimensional (clean) Fermi system with an attractive interaction above its critical temperature. While in the weak-coupling limit the standard analysis of superconducting fluctuations applies, we have shown that in the strong-coupling limit the original fermionic response functions become identical to the response functions of a system of composite bosons. We have, in fact, verified that only

those fermionic diagrams, to which there corresponds a meaningful representation in terms of composite bosons, contribute to the strong-coupling limit. The AL, MT, and fermionic DOS diagrams of superconducting fluctuation theory have been analyzed among others. We have also argued that the analysis of the spin response function may serve as a constraint to select sets of diagrams for the current and density response functions, which are relevant for weak coupling but are suppressed for strong coupling.

It is evident from our analysis that many diagrams contributing to the weak-coupling limit are suppressed in the strong-coupling limit. Consistently, by selecting the relevant diagrams for the response functions starting only from the strong-coupling limit, one might miss important contributions to the weak-coupling limit. For this reason, our analysis in the strong-coupling limit must be supplemented by the standard criterion of superconducting fluctuation theory for selecting suitable sets of diagrams in the weak-coupling limit. This is especially true for the spin response function, which vanishes for a system of spinless bosons. Extrapolating to the weak-coupling limit only diagrams which contribute in the bosonic limit to the current and density response functions, would in fact result into a vanishing spin response function for *all* coupling strengths.

Controlling the two (weak- and strong-coupling) limits separately may prove especially important for describing the intermediate (crossover) region, for which no controlled theory can be specifically formulated. One reasonable strategy to approach the crossover region is then to *interpolate* between two theories which are controlled, respectively, in the weak- and strong-coupling limits; this can be done by including all dominant diagrams in either one of the two limits and then evaluating them over the whole coupling range. This contrasts somewhat with what was found in reference [16] for the fermionic self-energy, for which a single approximation selected in the strong-coupling regime proved also sufficient to describe the weak-coupling region. For the response functions, at the leading order one may thus include the AL diagram (which is dominant both in the strong- and weak-coupling limits) plus the MT and fermionic DOS diagrams (which are relevant to the weak-coupling limit but are strongly suppressed in the strong-coupling limit). At the next-to-leading order, the effect of the residual interaction between composite bosons can be included considering the corrections to the AL diagrams discussed in Section 2.2, as well as the bosonic DOS diagram of Figure 7.

In this context, it is interesting to comment on the results reported in reference [27] regarding the temperature dependence of the density and spin susceptibilities for a two-dimensional negative-U Hubbard model, calculated *via* the AL, MT, and fermionic DOS diagrams, and then compared with available Monte Carlo results for  $U = -4t$  ( $t$  being the nearest-neighbor hopping). These authors find a remarkable agreement between their calculation and the Monte Carlo data for the spin susceptibility, *provided* the mass term in the particle-particle ladder (2.5) is replaced by a mass term with the characteristic temperature de-

pendence of the Kosterlitz-Thouless theory (a replacement that should amount to inserting self-energy corrections in the bosonic propagators of the AL diagram). For the density susceptibility, however, this replacement alone proved not sufficient to reproduce the Monte Carlo data. The discussion presented in Section 2.2 indeed suggests that modifications of the AL diagram obtained by considering bosonic self-energy corrections to the particle-particle ladder (*cf.* Fig. 7) should also be accompanied by the inclusion of an additional diagram (namely, diagram 4b for the density response function), which in the strong-coupling limit accounts for the residual bosonic interaction at the *same* order in the diluteness parameter for sufficiently high temperature. Our numerical calculations reported in Section 4 have indeed confirmed this expectation.

In this paper, we have considered the response functions in the normal phase *above* the critical temperature. It would certainly be interesting to extend this analysis *below* the superconducting critical temperature and study the continuous evolution of the response functions from the weak-coupling limit of (BCS) superconductivity to the strong-coupling limit where Bose-Einstein condensation takes place. In this case, a description in terms of Bogoliubov quasi-particles may be appropriate for a dilute system of composite bosons (at least close to zero temperature), with the superfluid density being affected at finite temperature by sound modes in the strong-coupling limit and by pair-breaking effects in the weak-coupling limit. Which of these two effects dominate in the intermediate (crossover) region is a challenging question, which can be addressed only by numerical calculations of suitable sets of diagrams. Work along these lines is in progress [28].

The authors are indebted to C. Castellani, A. Perali, and A. Varlamov for helpful discussions. Partial financial support from the Italian MIUR under contract Cofin/PRIN 1999 is gratefully acknowledged.

## References

1. J.R. Schrieffer, *Theory of Superconductivity* (Benjamin, New York, 1964)
2. See, *e.g.*, A.L. Fetter, J.D. Walecka, *Quantum Theory of Many-Particle Systems* (McGraw-Hill, New York, 1971), Chap. 13
3. L.G. Aslamazov, A.I. Larkin, *Sov. Phys. JETP* **10**, 875 (1968)
4. R.S. Thompson, *Phys. Rev. B* **1**, 327 (1970); J.P. Hurault, K. Maki, *Phys. Rev. B* **2**, 2560 (1970)
5. W.J. Skocpol, M. Tinkham, *Rep. Prog. Phys.* **38**, 1049 (1975)
6. A.A. Varlamov, G. Balestrino, E. Milani, D.V. Livanov, *Adv. Phys.* **48**, 655 (1999)
7. H. Ding *et al.*, *Nature* **382**, 51 (1996); and *Phys. Rev. Lett.* **78**, 2628 (1997)
8. A.G. Loeser *et al.*, *Science* **273**, 325 (1996)

9. A.J. Leggett, in *Modern Trends in the Theory of Condensed Matter*, edited by A. Pekalski, R. Przystawa, Lecture Notes in Physics Vol. 115 (Springer-Verlag, Berlin, 1980), p.13
10. P. Nozières, S. Schmitt-Rink, J. Low. Temp. Phys. **59**, 195 (1985)
11. C.A.R. Sá de Melo, M. Randeria, J.R. Engelbrecht, Phys. Rev. Lett. **71**, 3202 (1993)
12. R. Haussmann, Z. Phys. B **91**, 291 (1993)
13. F. Pistolesi, G.C. Strinati, Phys. Rev. B **49**, 6356 (1994); *ibid.* B **53**, 15168 (1996)
14. S. Stintzing, W. Zwerger, Phys. Rev. B **56**, 9004 (1997)
15. B. Jankó, J. Maly, K. Levin, Phys. Rev. B **56**, R11407 (1997)
16. P. Pieri, G.C. Strinati, Phys. Rev. B **61**, 15370 (2000), and `cond-mat/9811166`
17. V.N. Popov, *Functional Integrals and Collective Excitations* (Cambridge University Press, Cambridge, 1987)
18. G. Baym, in *Mathematical Methods in Solid State and Superfluid Theory*, edited by R.C. Clark, G.H. Derrick (Oliver and Boyd, Edinburg, 1967)
19. G. Baym, Phys. Rev. **127**, 1391 (1962)
20. It was shown in reference [16] that the scattering length  $a_B$  for composite bosons is proportional to the fermionic scattering length  $a_F$ , with a coefficient of order unity
21. P. Pieri, G.C. Strinati, I. Tifrea, Phys. Rev. B **64**, 52104 (2001)
22. In the strong-coupling (bosonic) limit, one may write  $\partial n/\partial\mu = 4 \partial n_B/\partial\mu_B$  and estimate  $\partial n_B/\partial\mu_B$  from the relation  $\mu_B(n_B)$  valid for an ideal Bose gas close to the Bose-Einstein temperature  $T_{BE}$  (*cf.* Ref. [2], Sect. 5). One obtains  $\partial\mu_B/\partial n_B \approx 1.63(T - T_{BE})/n_B$ , yielding a divergent  $\partial n_B/\partial\mu_B$  as  $T$  approaches  $T_{BE}$ , which further suppresses diagram 4(c) with respect to diagram 4b.
23. In the strong-coupling (bosonic) limit, the  $Q$  dependence of the MT and fermionic DOS diagrams is expected to be irrelevant insofar as the fermionic chemical potential constitutes the largest energy scale in the problem.
24. A similar cancellation has been noted in the weak-coupling limit by D.V. Livanov, G. Savona, A.A. Varlamov, Phys. Rev. B **62**, 8675 (2000)
25. M. Randeria, N. Trivedi, A. Moreo, R.T. Scalettar, Phys. Rev. Lett. **69**, 2001 (1992); J.M. Singer *et al.*, Phys. Rev. B **54**, 1286 (1996)
26. A. Perali, P. Pieri, G.C. Strinati, C. Castellani, Phys. Rev. B **66**, 024510 (2002)
27. L. Benfatto, A. Perali, C. Castellani, M. Grilli, Eur. Phys. J. B **13**, 609 (2000)
28. N. Andrenacci, P. Pieri, G.C. Strinati (unpublished)